The statistical flare

L. Vlahos, M. Georgoulis, R. Kluiving, and P. Paschos

Department of Physics, University of Thessaloniki, GR-54006 Thessaloniki, Greece

Abstract. Solar and stellar flares are interpreted so far as an instability of a large scale magnetic neutral sheet. In this article, however, we assume that the active region is highly inhomogeneous: a large number of magnetic loops are simultaneously present interacting and randomly forming discontinuities in many independent points in space. These magnetic discontinuities release energy and force weaker discontinuities in their neighbourhood to release energy as well. This complex dynamical system releases constantly energy in the form of small and large scale explosions. Clustering of many discontinuities in the same area has the effect of larger scale explosions (flares). This type of flare with spatiotemporal fragmentation and clustering in small and large scale structures will be called here the *statistical flare*.

The statistical flare is simulated using avalanche models originally introduced by Bak et al. (1988). Avalanche models applied so far to solar flares (Lu & Hamilton 1991) were isotropic (the field was distributed equally to the closest neighbours of an unstable point). These models simulate relatively large events (microflares and flares). Here we introduce a more refined isotropic avalanche model as well as an anisotropic avalanche model (energy is distributed only among the unstable point and those neighbours that develop gradients higher than a critical value). The anisotropic model simulates better the smaller events (nanoflares): in contrast to the well-known results of the isotropic model (a power law with index ~ -1.8 in the peak-luminosity distribution), the anisotropic model produces a much steeper power law with index ~ -3.5. Finally, we introduce a mixed model (a combination of isotropic and anisotropic models) which gives rise to two distinct power-law regions in the peak-luminosity distribution, one with index ~ -3.5 accounting for the small events, and one with index ~ -1.8 accounting for large events. This last model therefore explains coronal heating as well as flaring.

The three models introduced in this paper show length-scale invariant behaviour. Model-dependent memory effects are detected in the peak-luminosity time series produced by these models.

1. Introduction

Magnetic energy release in the sun and stars remains as one of the main unresolved problems in astrophysics. There are regions in the solar surface (called active regions) where magnetic fields are intense and highlly concentrated. Random motions in the photosphere split and move these fields in such a way as to enhance their mutual interactions and to form magnetic discontinuities. Understanding the evolution of these discontinuities will provide the key for solving the energy-release problem for the sun and stars.

Research on the possible forms of magnetic energy release in the sun and stars has been focused, so far, on two distinct subjects:

(a) Transport of energy along the magnetic field lines from the convection zone to the corona in the form of waves (Alfvén or magnetosonic waves) and subsequent dissipation in the corona (see the review by Zirker 1993).

(b) Magnetic storage and sudden release (triggering) which was termed as flare (see the review by Priest 1992).

These two processes have been studied in simple magnetic topologies e.g. solar loop, two interacting loops or well organised arcades of loops, since only then the problem was mathematically tractable. Isolating the two processes from the beginning and studying them in relatively simple topologies does not permit to see their interaction (wave propagation in highly inhomogeneous magnetic topologies (Sudan & Longcope 1990)) or generation of waves and shocks from reconnecting neutral sheets (Galsgaard & Nordlund 1994). Furthermore, research on the convection zone and photospheric motions has clearly shown that the "driver" of the active-region fields is turbulent. This implicates, in our view, that simplifications of the evolution of the magnetic topologies above the photosphere as mentioned above will not be representative for the real system.

Observations of the solar X-ray corona are apparent in the literature from the early seventies. These reports resulted from

many different ways of observation. With the present instrumental capabilities, observations show that the peak-luminosity distribution of flares displays a widely extended (over 3.5 orders of magnitude) power law with an index -1.80 ± 0.05 (Lin et al. 1984; Dennis 1985; Crosby et al. 1992; Pearce et al. 1993; Biesecker et al. 1994). Deviations from power-law behaviour however, are observed at lowest and highest energies. It has been stated that the lower deviation occurs due to instrumental limitations.

In the late eighties many scenaria were developed to explain the mechanism of energy input to the solar corona (see reviews by Heyvaerts 1990; Eunaudi & Velli 1994; Vlahos 1994). This input has been roughly estimated by Withbroe & Noyes (1977) to be about $10^7 [\mathrm{erg\ cm^{-2} s^{-1}}]$. This energy input is thought to be due to a continuous, small scale, localised dissipation of magnetic energy rather than to a few large events that release vast amounts of energy (Parker 1983; van Ballegooijen 1986; Berger 1993, 1994). Parker (1988) stresses that what we define as solar X-ray corona is just a tremendously large number of nanoflares.[1] Swarms of nanoflares in a localised region provide the essential energy input in the corona. According to Parker (1989), microflares observed are a result of a superposition of many nanoflares, while a superposition of a large number of microflares may give rise to the observational detection of a flare. This point of view results from the assumption that the same basic physics should hold for flares, microflares and nanoflares.

Lu & Hamilton (1991) and Lu et al. (1993) were the first to propose a different approach to the study of the active regions and the flaring process (LH model). They claimed that their model can be used to study the operative physics which leads to the large scale dynamics (and therefore the distribution of flares) in active regions. They assumed that the emergence as well as changes of magnetic flux in the photosphere place new flux at randomly located points inside the active region (magnetic loading of active region). This magnetic loading produces discontinuities in the magnetic field. Simple rules for the redistribution of magnetic field and the release of magnetic energy in the vicinity of a discontinuity are then applied. This model is able to predict a power-law behaviour for the number of discontinuities formed versus the total energy released. The power-law index obtained for peak-luminosity has a value of ~ -1.8 which is consistent with observations. Deviations from power-law behaviour obtained for lower and higher energies occur due to the finite resolution of the grid. The lower deviation is due to the cellular nature of the model, while the upper deviation is caused by the finite size of the simulation box.

Hudson (1991) showed that power-law distributions of peak luminosity with index ~ -1.8 fail to provide the energy needed to heat the corona. The power-law exponent should be ~ -4 to account for this heating. Due to the limitations of the current observational instruments, the existence of such a sharp power-

law fall-off in the lower part of the peak luminosity distribution has not yet been confirmed.

In this article the ideas of Parker and Hudson are reconciled following the approach of Lu and Hamilton. A number of new elements are introduced as compared to the original LH model: we enrich the (isotropic) LH model with more sophisticated instability criteria which provide for the relaxation of the (first and second order) neighbourhood of the initial unstable point. We obtain a (much more extended) power law in the peak-luminosity distribution with index ~ -1.8. Furthermore, we introduce an anisotropic model, which turns out to simulate smaller events and produces a power law with index ~ -3.5. Finally, we present a mixed model, which combines the two previous models. This model exhibits two distinct power-law regions in the peak-luminosity distribution, one with index ~ -3.5 (nanoflares) and one with index ~ -1.8 (microflares and flares). This last model, covering the entire range from nanoflares to flares, produces what we call in this article a statistical flare.

In Sect. 2 we introduce our alterations of the LH model and discuss the underlying physical motivation. In Sect. 3 and 4 we analyse the time series produced by our models and focus attention on correlations between subsequent events. In Sect. 5 we investigate the scaling behaviour exhibited by our models. Section 6 summarises our results.

2. Models for energy release in an evolving complex active region

We first review the basic principles of the LH model and briefly state the difference between these and those of our models. After that we explain in detail our models.

The LH model is based on the concept of self-organised criticality (SOC), first introduced by Bak et al. (1987). LH assume that the solar corona evolves into a SOC state, in which a single discontinuity (reconnection event) can trigger other similar events, giving rise to an avalanche. This swarm of events taking place almost simultaneously in a localised region is what we call a flare.

LH make use of an illustrative model which demonstrates SOC behaviour and is known as the 3D sandpile model.

Specifically, they construct a 3D cubical lattice with a vector field $\mathbf{F}_i$ associated with each grid point i. They define as "slope" the quantity

$$d\mathbf{F}_i = \mathbf{F}_i - \sum_j \omega_j \mathbf{F}_{i+j} , \qquad (1)$$

where ω_j is an arbitrary weighting function and $\mathbf{F}_{i+j}$ is the field of the six first-order neighbours of the grid point i. One introduces a critical threshold $\mathbf{F}_{\mathrm{cr}}$ and defines an instability criterion of the form

$$|d\mathbf{F}_i| > \mathbf{F}_{\mathrm{cr}} \qquad (2)$$

The algorithm consists in selecting randomly a grid point, adding to it a small increment $\delta\mathbf{F}$ with $\delta\mathbf{F} \ll \mathbf{F}_{\mathrm{cr}}$, and searching the grid for possible instabilities.

---

[1] Parker defines as "nanoflares" the practically unobservable events with energy $10^{24}[\mathrm{ergs}]$ or less and with highest energy up to $10^{26}[\mathrm{ergs}]$, which is our present observational limit.

If a grid point is found to be unstable, i.e. instability criterion (2) is satisfied, then itself and its neighbours are automatically readjusted in such a way that the field is conserved and the redistribution is isotropic (conservation laws and symmetry are established). At the same time an amount of energy (dependent on the slope $|d\mathbf{F}_i|$) is released. The grid is then again scanned, and if new instabilities are found, the same procedure of readjusting is applied. One keeps scanning the grid and readjusting the field until the system has relaxed onto a state in which no grid point is unstable. Then again a small increment $\delta\mathbf{F}$ is added to a randomly selected grid point and the same procedure of scanning and readjusting is applied.

This model predicts the prevalence of a power-law behaviour in the distribution functions of the total energy, the peak luminosity and the duration of the avalanches, extending over several decades. The consistency with observations leads to the conclusion that one might gain in this way an insight into the physics underlying the flaring mechanism.

We believe that the LH model is the first step towards the right direction of understanding flare emergence and flaring activity. The next step is to enrich the model with more realistic features, which is the subject of this article. Our models differ from the original LH model by the following items:

1. Whereas LH define size and peak activity of an avalanche using the total number of unstable points on which the avalanche extends, we define these quantities by directly making use of the energy released.
2. Whereas LH drive their model in a small scale ($|\delta\mathbf{F}| \ll \mathbf{F}_{cr}$), we use bigger increments, in accordance with the suggestion of Galsgaard & Nordlund (1994).
3. We load our grids with scalar fields instead of vector fields. By doing so we ignore energy placed in twisting magnetic fields.
4. We introduce three different models, one isotropic (Model A), one anisotropic (Model B) and one which is a combination of the previous two (Model C).
5. We introduce two generalised instability criteria (Criterion I and Criterion II) which are applicable to all three models.

We proceed now with a detailed description of our models.

2.1. Model A

We construct a three-dimensional cubical lattice at every grid point of which we define a scalar field B_i randomly selected from a fixed range of values. The slope at a grid point i is defined by

$$dB_i = B_i - \frac{1}{6}\sum_j B_{i+j} , \qquad (3)$$

where B_{i+j} is the field of the j-th first-order neighbour ($j = 1, 2, \ldots, 6$). The instability criterion has the form

$$dB_i > B_{cr} , \qquad (4)$$

where B_{cr} is the critical threshold. The typical value for B_{cr} was set on $B_{cr} = 50$.

Like the LH model, the procedure consists of selecting randomly a grid point, adding a small increment δB and scanning the whole grid for possible instabilities. The typical value for δB was set on $\delta B = 7$. If the instability criterion (4) is satisfied, the dynamical evolution of the system is given by the relations

$$B_i \rightarrow B_i - \frac{6}{7}B_{cr} \qquad (5)$$

$$B_{i+j} \rightarrow B_{i+j} + \frac{1}{7}B_{cr} \qquad (6)$$

where Eq. (5) provides the readjustments in the field of site i and Eq. (6) gives the readjustments in the fields of neighbouring sites $i + j$. First-order neighbours or first- and second-order neighbours (depending on the choice of the instability criterion, Criterion I or Criterion II) will then be checked for possible instabilities and, if any, they will be relaxed according to the rules of the specific instability criterion chosen. The two instability criteria are described in detail in Appendix I. Both criteria share the same philosophy: neighbours of an unstable point have relaxation criteria which depend on the strength of the instability of the initial point. The steeper the gradient, the easier the triggering of the neighbourhood is. Criterion I involves only first-order neighbours, while Criterion II takes first- and second-order neighbours into account.

On the other hand, maybe a neighbour satisfies directly criterion (4), so the relaxation mechanism (5) and (6) is again activated and the avalanche increases. When all avalanches acting within the limits of the lattice have died out, i.e. the system has become stationary, we repeat the routine of selecting randomly a grid point, adding the increment δB and so on. Each random selection and addition of the increment corresponds to what we call an iteration. Notice that symmetry and conservation laws are maintained, in agreement with the original SOC concept (Bak et al. 1987).

Once an instability has occurred, each readjustment of the field in the vicinity of the unstable point is accompanied by an elementary energy release given by the formula

$$\delta E_k = \left(B_k - \frac{6}{7}B_{cr} \right)^2 . \qquad (7)$$

Thus, if an avalanche is built of N relaxation events taken place in D time steps, then the total energy released is

$$E = \sum_{k=1}^{N} \delta E_k \qquad (8)$$

Time step is defined as the time needed for a single scanning of the grid including the relaxation of instabilities (if any).

The number of the relaxations at a specific time step multiplied by the elementary energy release (7) provides the peak luminosity P at this time step.

The total number of time steps from the onset of an avalanche to the total relaxation of the grid provides the duration D of this avalanche.

From the description given above it is clear that Model A follows closely the philosophy of the LH model, with exception, of course, of the introduction of the generalised instability criteria.

2.2. Model B

We construct a three-dimensional cubical lattice at every grid point of which we define a scalar field B_i randomly selected from a fixed range of values. Unlike Model A however, each grid point is characterised by *six* slopes instead of one. These slopes are defined by

$$dB_{ij} = B_i - B_{i+j} \ . \tag{9}$$

The instability criterion is now

$$dB_{ij} > B_{\mathrm{cr}} \ , \tag{10}$$

and it is applied six times for every grid point. For B_{cr} and δB the same values were used as in Model A. If criterion (10) is satisfied, only the grid point i and the neighbour j are involved in the relaxation process. Site i will rearrange its field following the rule

$$B_i \rightarrow B_i - \frac{6}{7} B_{\mathrm{cr}} \ . \tag{11}$$

If more than one dB_{ij} are greater than B_{cr}, then each one of the respective neighbours j will gain an increment δ_j with

$$B_{i+j} \rightarrow B_{i+j} + \delta_j \ , \tag{12}$$

provided that

$$\sum_j \delta_j = \frac{6}{7} B_{\mathrm{cr}} \ , \tag{13}$$

and

$$\delta_j = \frac{6}{7} B_{\mathrm{cr}} \frac{dB_{ij}}{\sum_j dB_{ij}} \ . \tag{14}$$

Either Criterion I or Criterion II is applied in the relaxation process. Definitions of total energy E, peak luminosity P and duration D are the same as in Model A.

It is clear that Model B provides a different philosophy as compared to Model A:

- Model B is clearly anisotropic. The relaxation procedure provides a directionality towards the neighbour or the neighbours that need to be readjusted according to the instability criterion (10). In other words, instability in this model finds its way out, instead of being isotropically distributed.
- From the theoretical point of view, Model B deviates from the original SOC concept: though conservation laws are maintained, symmetry is violated.

2.3. Model C

This model is simply a combination of the two previous models. We keep the common features of Models A and B, namely we randomly choose one grid point i per iteration and add the increment δB. The distinguishing feature, however, is that in obtaining a Model C time series, we just superimpose two time series, one constructed according to the rules of Model A and one constructed according to the rules of Model B. Here Model A and Model B share the same general features (same size of the simulation box, same critical threshold, same instability criterion, and same number of random selections of a point and additions of the increment).

The physical motivation for this superposition stems from the idea that our simulation box (of size L) represents only a very small fraction of the active region which, due to certain limitations of the observational instruments, cannot be detected. Instead, one detects a part of the corona which has a much bigger volume than our simulation box. If in this volume large isotropic explosions as well as small anisotropic events take place, then a correct modelling of this volume would require a number, say N_A, of Model A simulation boxes as well as a number, say N_B of Model B simulation boxes. The time series stemming from observations is then modelled by adding N_A Model A time series to N_B Model B time series. In a first approximation to this type of modelling we choose $N_A = N_B = 1$.

Obviously, our Model C is only a first approach to the problem. A much more natural model which is at present under consideration and will be presented in a later publication, is based on the philosophy of allowing the physics to decide how to relax discontinuities. The idea is that, if there is a discontinuity which leads to the fulfilment of the isotropic instability criterion (4), then the energy release will take place isotropically creating large events (flares). If, on the other hand, the gradients are steep enough to satisfy at least once anisotropic criterion (10), but not steep enough to give rise to a large isotropic explosion, then dissipation of energy will indeed take place, but this time it will lead to the emergence of nanoflares.

Even with our simple Model C however, the results are pretty encouraging as will be shown in Sect. 3.3.

3. Flare statistics

We first discuss some general features of our models.

Figure 1 shows a Model A simulation box with dimensions $50 \times 50 \times 50$ after 100 time steps. It includes clusters of different sizes, indicating the sizes of the avalanches to which they correspond. Notice that there are clusters consisting of only a single unstable point, which means that this point was randomly chosen at a time, but the disturbance was not able to spread to the vicinity of this point. On the other hand, there are clusters including a considerable number of points, indicating that the neighbourhood of the initial unstable point was affected by the relaxation process (spontaneous triggering of flare).
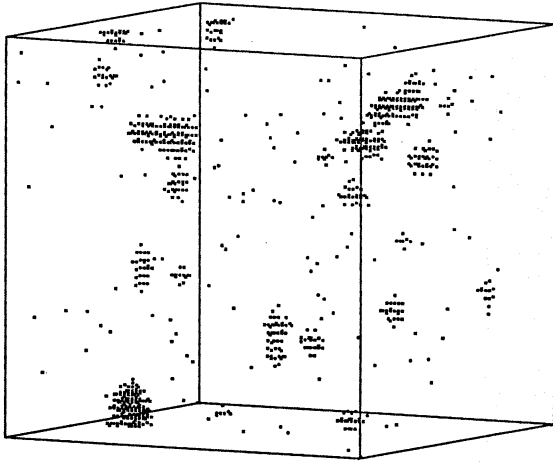
Fig. 1. Three-dimensional Model A simulation box with dimensions $50 \times 50 \times 50$ illustrating the clustering of unstable points (avalanches) after 100 time steps

Fig. 2. a Surface plot of the field magnitudes for a cross-section of a $10 \times 10 \times 10$ grid. **b** The same surface plot after the relaxation of gradients using Model A criteria. I denotes an isotropic gradient, whereas A denotes an anisotropic one

The relaxation of a single discontinuity is illustrated in Fig. 2. We have taken a cross-section (slice) of a $10 \times 10 \times 10$ grid and plotted the field of every grid point of the surface.

The large discontinuity at site $(5,7)$, marked by I, is clearly apparent in Fig. 2a. Figure 2b provides the same picture after the relaxation of the gradients. In this figure the shapes of the neighbouring peaks have changed, indicating that each one of them has received field from the highest peak, which has now disappeared. All the peaks now have heights below the critical threshold. Notice that the anisotropic discontinuity at $(8,4)$, marked by A, has remained unchanged.

We proceed with stating the results of each of our models.

3.1. Model A

As it turns out, the results are not affected by the particular choice of the instability criterion (Criterion I or Criterion II). The basic feature of both models is that the frequency distribution of energy E, peak luminosity P and duration D of the avalanches are well fitted by a functional form

$$N(X) = X^{-\delta_X} , \qquad (15)$$

where $X = E, P, D$. The exponent δ_X is the same[2] for both Criterion I and Criterion II for a fixed X. These power laws are the most extended for the energy E, and the least extended for the duration D, cf. Fig. 3.

In Fig. 3a comparison with the LH model is given. For the LH model we have used the energy release formula (7). Notice that the introduction of Criterion I or Criterion II forces the power-law regime to extend dramatically, without any serious difference in power-law indices. Power-law indices for grids with linear dimensions varying from 30 to 100 are given in Table 1. The values tabulated in Table 1 correspond to Criterion

Table 1. Power-law indices for total energy E, peak luminosity P and duration D for Model A grids of different size. Each index is an average taken over ten runs of 22000 time steps

L	δ_E	δ_P	δ_D
30	1.65	1.82	2.57
40	1.65	1.82	2.74
50	1.65	1.90	2.42
60	1.66	1.84	2.63
70	1.63	1.89	2.56
80	1.60	1.84	2.56
90	1.60	1.76	2.32
100	1.59	1.88	2.34

---

[2] The only difference between Criterion I and Criterion II is that the latter gives rise to the emergence of slightly larger events. This however does not affect the value of the exponent in Eq. (15)
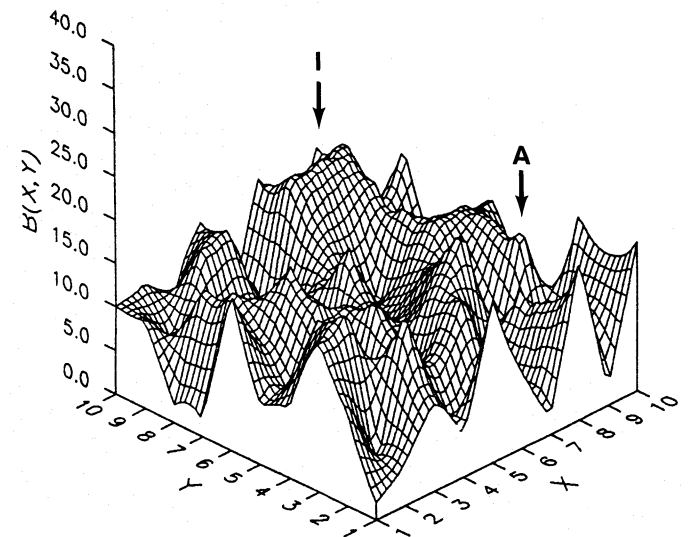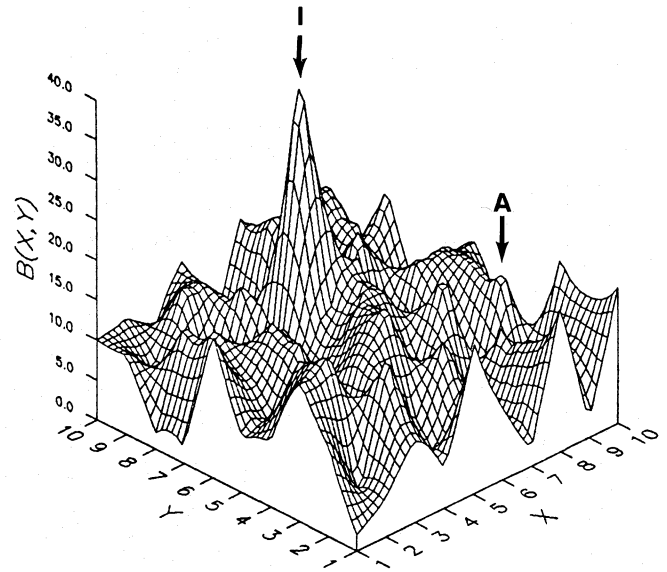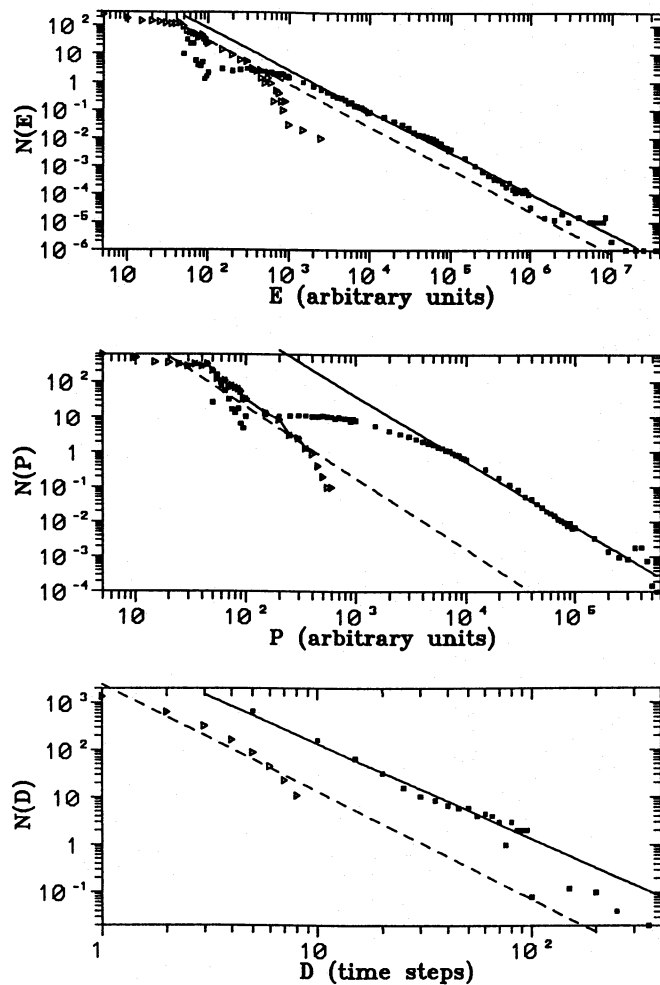
Fig. 3a–c. Frequency distributions of **a** energy E, **b** peak luminosity P and **c** duration D of the avalanches in a $100 \times 100 \times 100$ Model A grid. The triangles correspond to the results of a model using exactly the same criterion as the LH model

II but do not differ significantly (in a statistical sense) from the values corresponding to Criterion I. From our statistical analysis we obtain the following numerical results:

1. A power-law index for energy with value $\sim -1.62 \pm 0.03$.
2. A power-law index for peak-luminosity with value $\sim -1.84 \pm 0.04$.
3. A power-law index for duration with value $\sim -2.5 \pm 0.1$.

We remark that these exponents are insensitive to the randomly chosen initial configuration of the field and to the value of the increment δB provided that the latter is not bigger than 20 % of the critical threshold.

The quantity which can directly be compared with observations is the peak-luminosity P. The power-law index -1.84 is consistent with observations. The power-law index for energy is slightly higher than the index provided by the LH model. There is some ambiguity in determining the power-law index for the the duration distribution. This is due to the fact that the extension of this power-law is not big enough to allow for an accurate power-law fitting (Fig. 3c).

We also observe certain deviations from power-law behaviour at the lowest and highest energies (Fig. 3a,b). Explanations for these deviations have already been mentioned in the introduction.

Model A is rather similar to the LH model. But we find ourselves in contradiction with the assertion of LH that power-law scaling is not obtained if one lowers the instability criterion (4) or forces the neighbouring sites to undergo relaxation. Instability Criteria I and II are based on the philosophy of forcing the vicinity of the unstable point to relax, in this way attempting to simulate realistic conditions acting in the solar corona (Galsgaard & Nordlund 1994). We do obtain power laws, and find that the power-law indices are consistent with those of the LH model.

3.2. Model B

The first conclusion drawn from our simulations is that the results are not affected by choosing either Criterion I or Criterion II. The second conclusion is that the behaviour of Model B deviates significantly from that of Model A.

The basic feature, which can be directly read off from a typical model B time series (Fig. 4b) is the occurrence of swarms of small and short events. The energy scale of these events is some orders of magnitude less than the scale of events obtained from Model A (Fig. 4a).

In Fig. 4a a typical Model A time series is presented. Notice that the Model B time series of Fig. 4b displays a much more complex microstructure than Model A. The form of the Model B time series is explained by the fact that now (magnetic) energy cannot be stored in big quantities in a single lattice site or in its neighbourhood. It dissipates much easily than in the isotropic model (Model A), since only the unstable point and one neighbour are needed for an event to occur. This fact contributes to a picture of a very frequent, small localised dissipation of energy, instead of the prevalence of a few enormous events which release the vast majority of energy available (Model A). The two pictures are apparent in Fig. 5a,b.

Figure 5a corresponds to a $50 \times 50 \times 50$ Model A simulation box, while Fig. 5b shows the simulation box of a system with the same size exhibiting Model B behaviour.

The different simulation rules are reflected by the frequency distributions of energy and peak luminosity. Typical distributions for a $100 \times 100 \times 100$ Model B are given in Fig. 6. Notice that the distributions of energy and peak luminosity begin with a plateau of roughly constant occurrence rates and terminate in a sharp cut-off. The slopes of these cut-offs are significantly higher than in Model A. Their absolute values are given in Table 2 for a range of lattice sizes varying from $(30)^3$ till $(100)^3$.

From our analysis we conclude:

1. We obtain a cut-off for the energy E with a power-law index $\sim -3.4 \pm 0.1$.
2. The cut-off of the peak luminosity P exhibits a power-law index of $\sim -3.65 \pm 0.10$.
3. The cut-off of the duration D distribution is really very steep, having an index $\sim -8.5 \pm 1.5$.
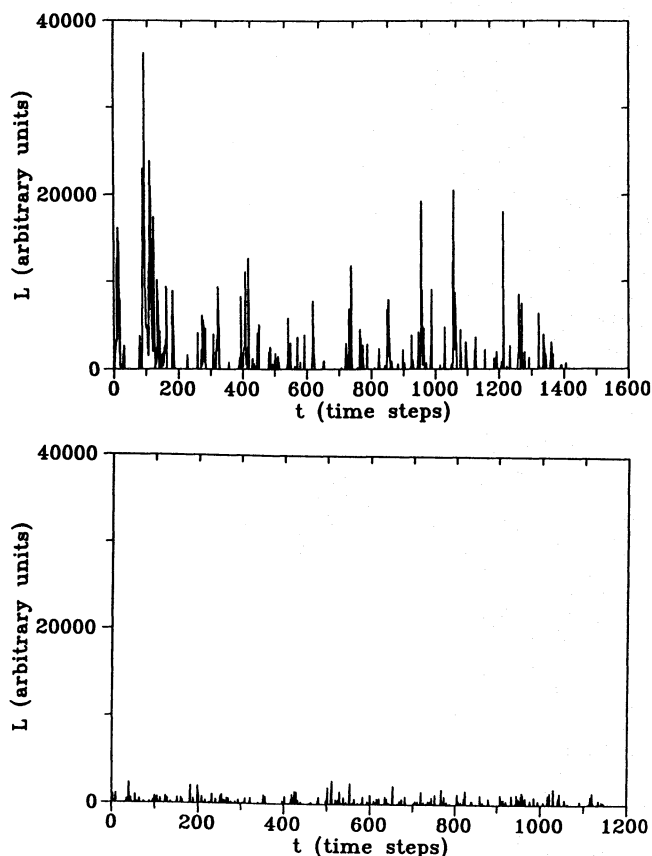
Fig. 4a and b. Typical time series of **a** Model A behaviour (microflares and flares), **b** Model B behaviour (nanoflares)

Table 2. Power-law indices for the total energy E, peak luminosity P and duration D for a number of Model B grids of different sizes. Each index is an average taken over ten runs of 22000 time steps.

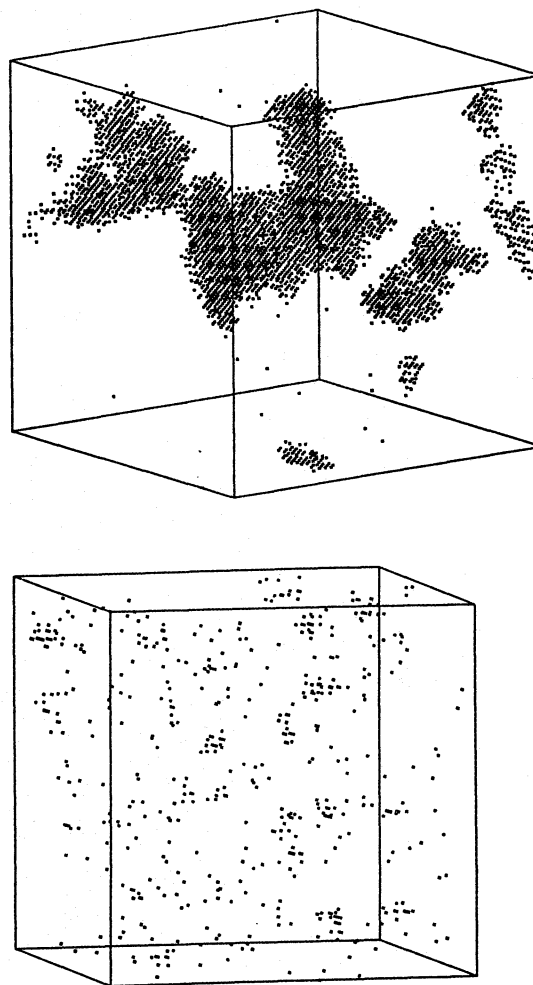| L	δ_E	δ_P	δ_D
30	3.55	3.61	7.32
40	3.34	3.74	7.28
50	3.36	3.82	7.14
60	3.35	3.59	7.31
70	3.43	3.60	7.39
80	3.56	3.60	10.66
90	3.41	3.54	11.38
100	3.56	3.72	11.41

Fig. 5a and b. $50 \times 50 \times 50$ simulation boxes which show the emergence of events (avalanches) after 100 time steps for **a** Model A and **b** for Model B

threshold, the shorter the extension of the plateau with the cut-off index remaining practically unchanged.

Model B represents the relaxation processes which give rise to small events (nanoflares). In fact, Model B materialises the ideas expressed by Hudson (1991) and Zirker & Cleveland (1993a and b). We conclude that small and short events (nanoflares) originate from anisotropy while isotropy governs the emergence of large events (microflares and flares).

3.3. Model C

In Fig. 7 a time series of Model A (Fig. 7a) and a time series of Model B (Fig. 7b) are added to create a Model C time series (Fig. 7c). We see that this Model C time series exhibits large events (due to Model A) embedded in an active background of small events (due to Model B). This picture is, in our view, more realistic than those of Fig. 7a or b.

The energy, peak luminosity and duration distributions for a $100 \times 100 \times 100$ Model C grid are given in Fig. 8. For the
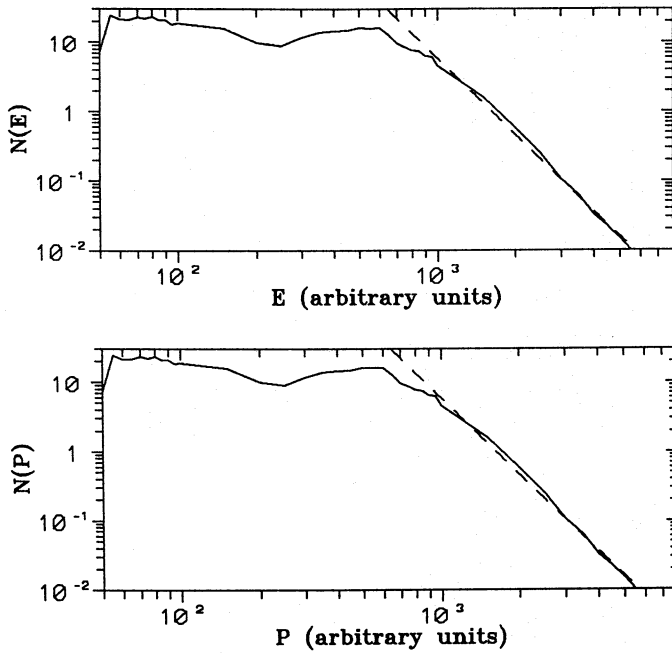
Notice that the distributions of the energy E and the peak luminosity P resemble each other very much due to the fact that we obtain short-duration events.

The general features of Model B are the same as those of Model A. The initial configuration of the field does not affect the results, and the cut-off index is insensitive to the increment δB as long as this increment is not bigger than 20 % of the critical threshold. We use the same values of δB and B_{cr} as in Model A.

The plateau which is observed in Fig. 6a and b *is strongly dependent on the critical threshold used.* The lower the critical

Fig. 6a and b. Frequency distributions of **a** energy and **b** peak luminosity for a 100 × 100 × 100 Model B grid
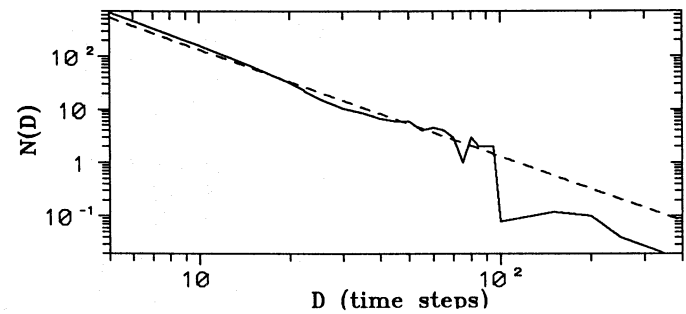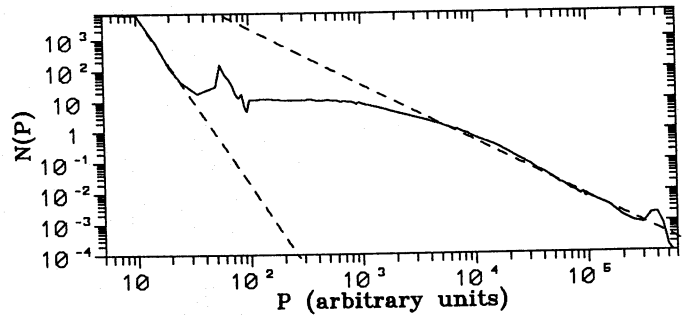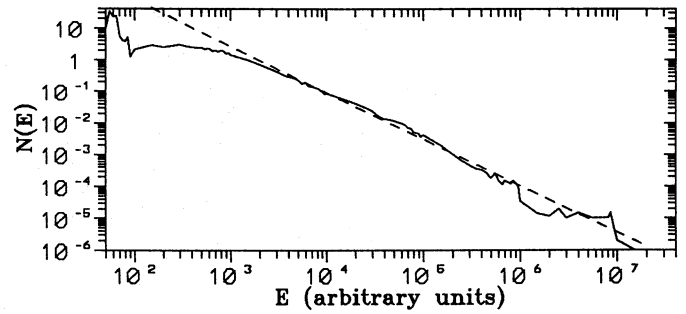

Fig. 8a–c. Frequency distributions of **a** energy, **b** peak luminosity and **c** duration for a 100 × 100 × 100 Model C grid

energy distribution (Fig. 8a) the power-law behaviour is exactly the same as the power-law behaviour of Model A (Fig. 3a). All the events presented by the power-law are strictly isotropic. Small anisotropic events affect only lowest energies, below the threshold above which power-law scaling appears. Indeed, the only difference between Fig. 8a and Fig. 3a is located exactly at these lowest energies.

The distribution of peak luminosity however (Fig. 8b) exhibits different behaviour. Isotropic events last for relatively many time steps. So isotropic luminosities have significantly lower values than isotropic total energies, in this way permitting anisotropic events to become more visible as compared to the energy distribution. Direct consequence is the emergence of two scaling regions (Fig. 8b): the low-energy region which has the sharp Model B index as in Fig. 6b and the high-energy region which is strictly isotropic, with the same index as in Fig. 3b. We believe that the occurrence of two scaling regions reflects the simultaneous presence of two phenomena: flare production and coronal heating.
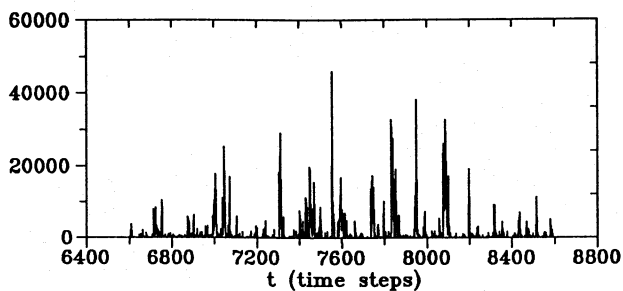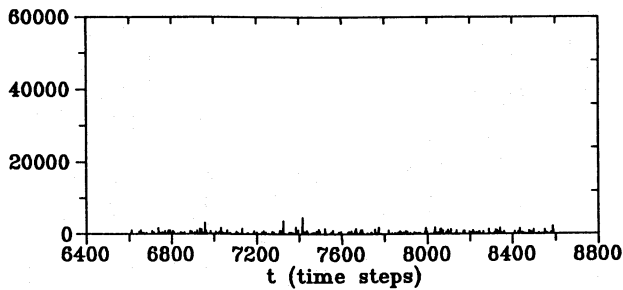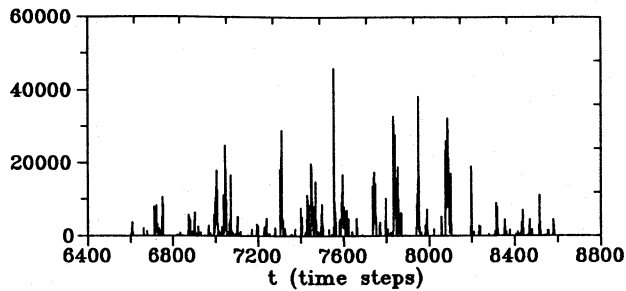

Fig. 7a–c. The construction of a Model C time series (**c**) by the superposition of a Model A time series (**a**) and a Model B time series (**b**) for a 50 × 50 × 50 grid

The duration distribution of Model A (Fig. 3c) remains practically unaffected by the superposition of the Model B duration distribution. Thus Fig. 8c is almost exactly the same as Fig. 3c.

4. Correlations

Here we discuss the issue of correlation between relaxation events using basic concepts taken from the theory of multi-fractals (Hentschel & Procaccia 1983; Halsey et al. 1986; Tél 1988).

When a peak-luminosity time series is given, and one wants to examine the self-similarity (multifractality) of this time series, the most straightforward method is the box-counting method: If N denotes the length of the time series, one covers the time axis with a grid of boxes, each having the same size λ. Expressing the box size λ using N as the unit length, the time series is covered by N/λ boxes with (dimensionless) size $\varepsilon = \lambda/N$. The normalised peak luminosity $\tilde{P}_i$ of a box i (i running from 1 till N/λ) is defined as the sum of the λ peak luminosities inside this box divided by a normalising factor. The normalising factor is equal to the sum of all N peak luminosities. Since the sum of all normalised peak luminosities $\tilde{P}_i$ is equal to 1, $\tilde{P}_i$ can be called a probability.

In most cases of interest, the sum $\sum_i \tilde{P}_i^q(\varepsilon)$ of the probabilities raised to the power q exhibits the following scaling behaviour:

$$\sum_i \tilde{P}_i^q(\varepsilon) \sim \varepsilon^{(q-1)D(q)} . \tag{16}$$

In relation (16) $D(q)$ corresponds to the generalised dimensions of the time series which depend on the value of the quantity q which is called "selector". In case of multifractality, each value of the selector q corresponds to a different value of $D(q)$ where $D(q) \geq D(q')$ if $q < q'$, i.e. $D(q)$ is a decreasing function. The best-known generalised dimensions characterising a probability distribution are $D(0)$ which is named "fractal dimension" and $D(2)$ which is called "correlation dimension".

More generally, the generalised dimensions $D(n)$ with $n = 2, 3, 4, \ldots$ are related to the n-tuplet (point) correlation integral $C_n(\varepsilon)$ by (Hentschel & Procaccia 1983):

$$D(n) = \frac{\log C_n(\varepsilon)}{\log \varepsilon} \tag{17}$$

In the context of this subsection, a "point" corresponds to a relaxation event and the normalised peak luminosity $\tilde{P}_i$ is to be interpreted as the (normalised) number of relaxation events at time step i. A value of $D(n)$ equal to 1 corresponds to the absence of correlations in a group of n consecutive relaxation events. A value of $D(n)$ smaller than 1 indicates that, on the average, correlation (memory) effects are present within a cluster of n subsequent relaxation events.

The accuracy of the box counting method depends on the two parameters λ and N which are united in the single parameter $\varepsilon = \lambda/N \ll 1$. The box-counting method is only reliable if for decreasing values of ε relation (16) holds over several order
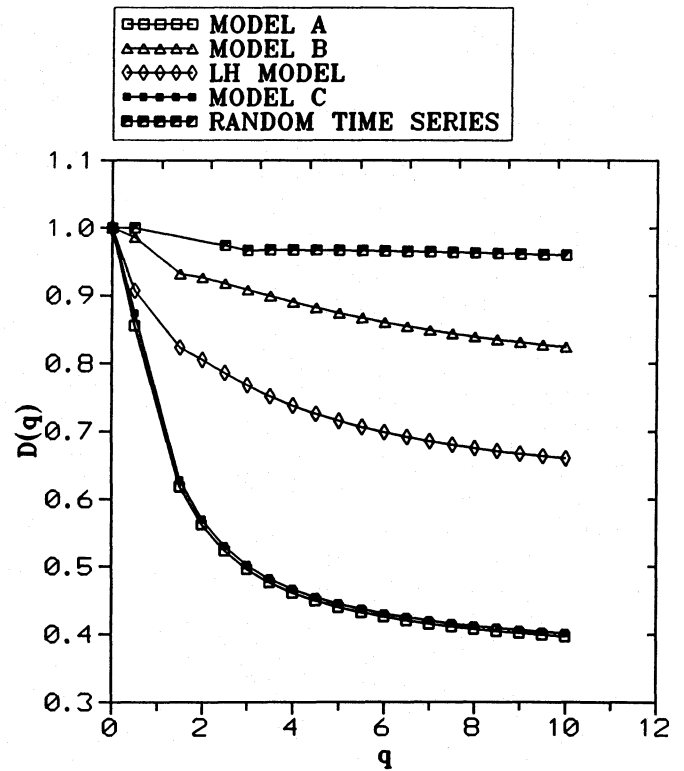

Fig. 9. $D(q)$ curves for a random time series, LH model and Models A, B, and C for a $100 \times 100 \times 100$ grid. The curves for Model A and Model C are almost coincident

decades of $\log \varepsilon$. In some cases, convergence is only reached in the limit $\varepsilon \to 0$.

It is well known that it is almost impossible to obtain accurate estimates of the negative q-part of the $D(q)$ curve, since the inevitable round-off error in the values for the probabilities $\tilde{P}_i$ is blown up in the left hand side of Eq. (16). This is the reason why in our analysis we have avoided negative q values. Another reason is that the negative-q part of the $D(q)$ spectrum provides no information about correlations. In fact, a physical interpretation of this part of the spectrum is still lacking.

The selfsimilar (fractal) nature of the avalanche models exhibiting SOC behaviour is stressed by several authors (Bak et al. 1987,1988; Bak & Chen 1991). This selfsimilarity with a scale-invariant behaviour is believed to cause the emergence of power-laws.

The $D(q)$ spectra for typical peak-luminosity time series of Model A, Model B and Model C grids are shown in Fig. 9. We also have plotted the $D(q)$ spectrum of the LH model and, to illustrate the difference between events with no correlation, we have plotted the $D(q)$ spectrum of a totally random time series.

Clearly, the $D(q)$ spectrum of the random time series is flat, i.e. $D(q)$ has almost the same value for different values of q. This value deviates slightly from the exact value 1, since the length of the random time series was not infinite, but kept the same as the length of the time series resulting from our models ($N = 22000$).

We further see that the Model-B curve is close to the "random"-curve, indicating that correlation effects are weak. The curves corresponding to Model A and Model C are almost coincident and deviate convincingly from the "random" curve, indicating the existence of relatively strong correlation effects in the associated time series. That the Model-A curve lies beneath the Model-B curve is explained by the observation that flares (long and strong energy bursts) are dominant in Model A and absent in Model B (which displays only short and weak bursts (nanoflares)). Therefore one expects correlations to be much stronger in Model-A time series as compared to Model-B time series. This is exactly what one sees in Fig. 9. The fact that the Model-A curve coincides with the Model-C time series also has a simple explanation: correlations depend on the strongest and longest bursts. Since these strongest and longest bursts are the same for both Model A and Model C (since Model C is simply a superposition of Model A and the shortly and weakly bursting Model B), both models display the same correlation behaviour.

Notice that the $D(q)$ curve of the LH model lies somewhere between the Model-B curve and the Model-A/Model-C curve.

We conclude that we have found evidence for the existence of correlations between relaxation events in Model A and Model C, while, on the other hand, correlations in Model B relaxation events are relatively weak. The LH model appears to have an intermediate degree of correlation. Our analysis clearly shows that there is model-dependent memory effect in our time series.

We recommend the same method of analysis introduced in this section for observational time series in order for modellists to compare their data more accurately with observations.

5. Scaling

We will now turn to the scaling behaviour of our models, i.e. we want to investigate whether the distribution functions of our models display a length-scale invariant behaviour for grid-sizes $L = 60$ up to $L = 100$. If this is true, then the same length-scale invariant behaviour can be expected for grids with sizes which are too large for numerical verification.

The relevance of this topic is evident: a correct modelling of flare phenomena in the corona would require huge gridsizes, which, however, are completely inaccessible to numerical simulations with the currently available computers. Therefore, the only way to be confident that models which are successful for relatively small gridsizes are also successful for very large gridsizes, is to search for length-scale invariant behaviour of the relevant distribution functions.

In connection to this it is important to notice that the observation done in Sects. 3.1 and 3.2, namely that the power-law indices associated with the various distribution functions display a length-scale invariant behaviour (Tables 1 and 2), is insufficient for predicting that the *entire* distribution function is length-scale invariant: the power-law indices result from a power-law *fit*, and it could well be possible that the range of values over which the power-law approximation extends depends on the size of the grid. More precisely, *we require that also the deviations from power-law behaviour display a length-scale in-*

variant behaviour. We only allow deviations at the borders of the interval over which the distribution function extends. As already stated in the introduction, the lower deviation is due to the cellular nature of the models, while the upper deviation is caused by the finite size of the grid.

In order to investigate the scaling behaviour of our models, we apply three different tools: finite-size scaling (Fischer 1971; Barber 1984), multiscaling (Kadanoff et al. 1989) and multifractal scaling (Appendix II).

If one has a set of distribution functions, each of which is associated with a simulation box of different size L, then each of the three tools mentioned above tries to map these functions onto a single "universal" curve. If this is possible, then the model is said to show common behaviour independent of L.

Kadanof et al. (1989) studied the scaling behaviour of several one- and two-dimensional avalanche models by means of finite-size scaling and multiscaling analysis (which in their original article was erroneously[3] coined "multifractal scaling"). Here we extend the analysis of Kadanoff et al. to our three-dimensional avalanche models. Let us first explain briefly the three tools of analysis.

5.1. Description of tools

1. **Finite-size scaling**. For different sizes L one tries to express the distribution functions $N(X, L)$ as follows:

$$N(X, L) = L^{-\beta} f_1(X/L^{-\nu}) , \qquad (18)$$

where $X = E, P, D$. Expression (18) is called a finite-size scaling form, because it depends on two critical scaling indices, β and ν. The function f_1 is called a scaling function. If the distribution functions are dominated by a long region of power-law behaviour with power-law index δ, then δ is related to β and ν via (Kadanoff et al. 1989)

$$\delta = \beta/\nu , \qquad (19)$$

while β and ν are related to each other by

$$2\nu - \beta = 3 . \qquad (20)$$

2. **Multiscaling**. The multiscaling fitting form (Kadanoff et al. 1989) is given by

$$\frac{\log N(X, L)}{\log(L/L_0)} = f_2(\alpha) \text{ where } \alpha = \frac{\log(X/X_0)}{\log(L/L_0)} \qquad (21)$$

and L_0 and E_0 are fitting constants. The form (21) is called multiscaling form, because now an entire spectrum of scaling indices arises. These indices correspond to the values of the derivatives $df_2/d\alpha$. If the distribution functions are dominated by a long region of power-law behaviour, then the scaling function f_2 is a linear function of α.

3. **Multifractal scaling**. A new[4] method comes directly from the theory of multifractals (see Appendix II). This fitting form is different as compared to the multiscaling fitting form (21), and is given by the relation

$$\frac{\log(N(X, L)/N_0)}{\log L} = f_3(\alpha) \text{ where } \alpha = \frac{\log(X_0/X)}{\log L} \qquad (22)$$

---

[3]   See the last paragraph of Appendix II
[4]   See, however, ref. 12 in Kadanoff et al. 1989

and N_0 and X_0 are fitting constants. Notice that the multifractal fit (22) corresponds also to a type of multiscaling fit. Again, if the distribution functions are dominated by a power-law behaviour, then $f_3(\alpha)$ is linear.

The reason for using three fitting forms is that it is a priori unknown which of the three fitting methods will be successful: for one-dimensional avalanche models it was found by Kadanoff et al. (1989) that finite-size scaling works poorly as compared to multiscaling. For their two-dimensional avalanche models on the other hand, it was found that finite-size scaling works slightly better than multiscaling.

5.2. Results

Each model (Model A, Model B or Model C) is characterised by three types of distribution functions: Energy distribution, peak-luminosity distribution and duration distribution. Since of these distribution functions, the energy distribution is the most extended, we feel that it is the most appropriate distribution function for testing the length-scale invariance of our models. Length-scale invariant behaviour in terms of peak-luminosity and duration distribution will be discussed by us in a forthcoming publication.

5.2.1. Model A

We apply the three tools of analysis to the energy distribution. The scaling functions f of Eqs. (18), (21) and (22) are presented in Fig. 10.

From Fig. 10 we conclude that the length-scale invariant behaviour of Model A is ruled by the multiscaling form (21) as well as by the multifractal scaling form (22) and it is difficult to say which method works better. The multiscaling fit displays only slight deviations in the high-energy part of the distributions, while the multifractal fit shows deviations only in the low-energy part of the distributions. Notice that both fits show a clear multiscaling, the fitting curves are bended. The immediate conclusion is that the characterization of Model A energy distributions by means of a power-law fit (with index ~ -1.8) is, from the theoretical point of view, a gross simplification. Model A can be characterized by either a universal curve corresponding to the multiscaling fitting form (21) or by a universal curve corresponding to the multifractal fitting form (22).

The finite-size fitting form (18) works poorly as compared to the other two fitting forms. Clearly, the length-scale invariant behaviour of Model A is not ruled by finite-size scaling.

5.2.2. Model B

The three fitting forms for the energy distributions of Model B are presented in Figs. 11a, b and c.

From these figures we conclude that the multiscaling fitting form (21) gives the most convincing fit over the entire energy range. The multifractal fit works poorly in the low-energy part of the distributions, but works better in the power-law regime as compared to the multiscaling fit. Notice that, as could be
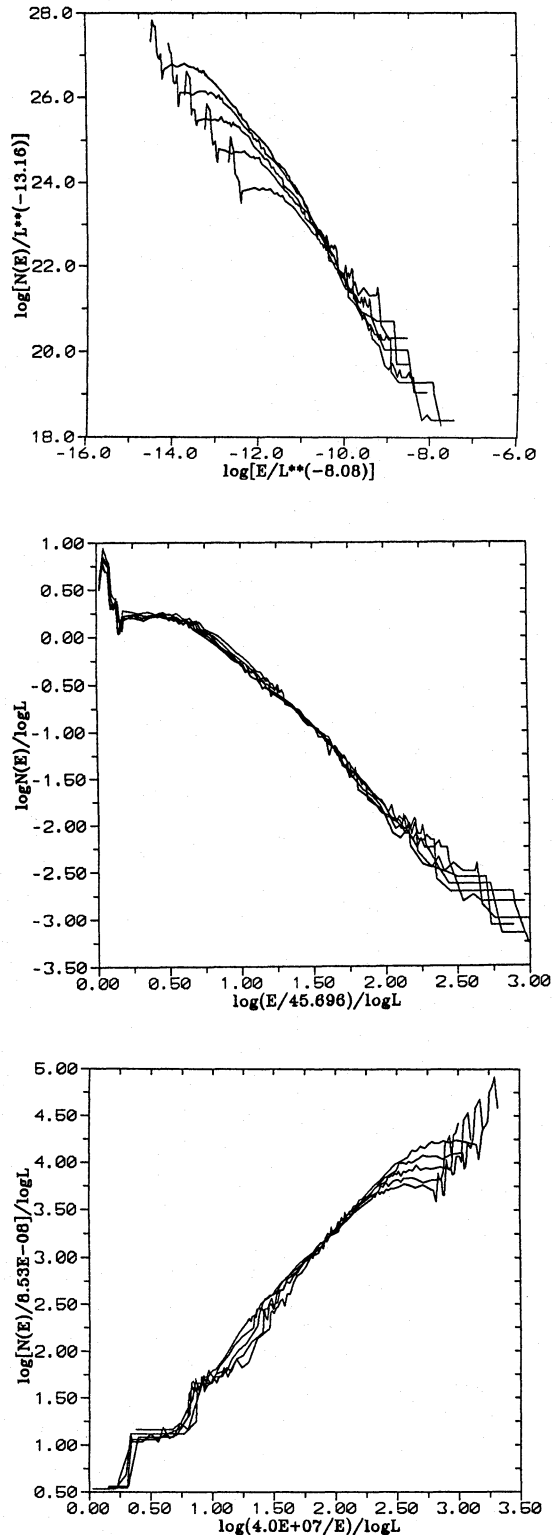

Fig. 10a–c. Scaling fits for the energy distributions (L =60, 70, 80, 90, 100) of Model A: **a** Finite-size scaling fit, **b** Multiscaling fit and **c** Multifractal scaling fit. The finite-size scaling fit works poorly as compared to the multiscaling and the multifractal fit. The multiscaling fit works good, deviations occur only for high energies. The same is true for the multifractal fit, but here the deviations from proper scaling occur only for low energies

expected, all three fitting forms work more or less well in the sharp power-law fall-off region of the distributions.

The good result of the multiscaling fitting (21) indicates that also for Model B the characterization by means of a single power-law exponent is a gross simplifaction: Model B can be characterised by a universal scaling function.

5.2.3. Model C

As was explained in Sect. 3.3, the energy distribution for Model C is equal to the energy distribution of Model A. The scaling fits for Model C are therefore the same as those for Model A. In a more technical language, this means that Model A and Model C belong to the same universality class.

In summary, the energy-distribution functions of all three models display length-scale invariant behaviour: the distributions can be scaled on a bended "universal" curve.

6. Summary and conclusions

Up till now, research on solar flares has evolved around concepts like magnetic storage (due to organised motions in the photosphere), formation of neutral sheets in well behaved magnetic topologies, plasma heating and acceleration of particles inside magnetic loops. The *statistical flare* introduced in this article replaces these concepts by random magnetic field loading of a complex active region, random formation of discontinuities, automatic relaxation of discontinuities, formation of clusters (avalanches) and heating and acceleration of particles on random discontinuities. In our view the statistical flare represents better inhomogeneous magnetic fields driven by turbulent motions in convection zone and photosphere.

In this article the evolution of the statistical flare is modelled using techniques taken from complex systems theory. Specifically, the occurrence, evolution and disappearance of sharp magnetic gradients driving currents which redistribute the magnetic fields and release energy is modelled using 3D avalanche models in the spirit of Lu & Hamilton (1991) and Lu et al. (1993).

Our main result is that our most successful model (Model C) provides a peak-luminosity distribution which exhibits two regions of power-law behaviour: a low-energy region with power-law index ~ -3.5 and a high-energy region with power-law index ~ -1.8. We stress that this result is in accordance with the assertion of Hudson (1991) (who states that a peak-luminosity power-law index of ~ -4 is needed to account for coronal heating) and with observations (which provide a power-law index of ~ -1.8 for the peak-luminosity distribution above the observational threshold). We repeat, however, that the steep power-law with index ~ -4 has not yet been observed.

In modelling the statistical flare, we introduced a number of new concepts which can be summarised as follows:

1. We termed the LH model as "isotropic" since the magnetic field is distributed equally among the six first-order neighbours. Our isotropic model differs from the LH model in the instability criteria. We assumed that if a specific point
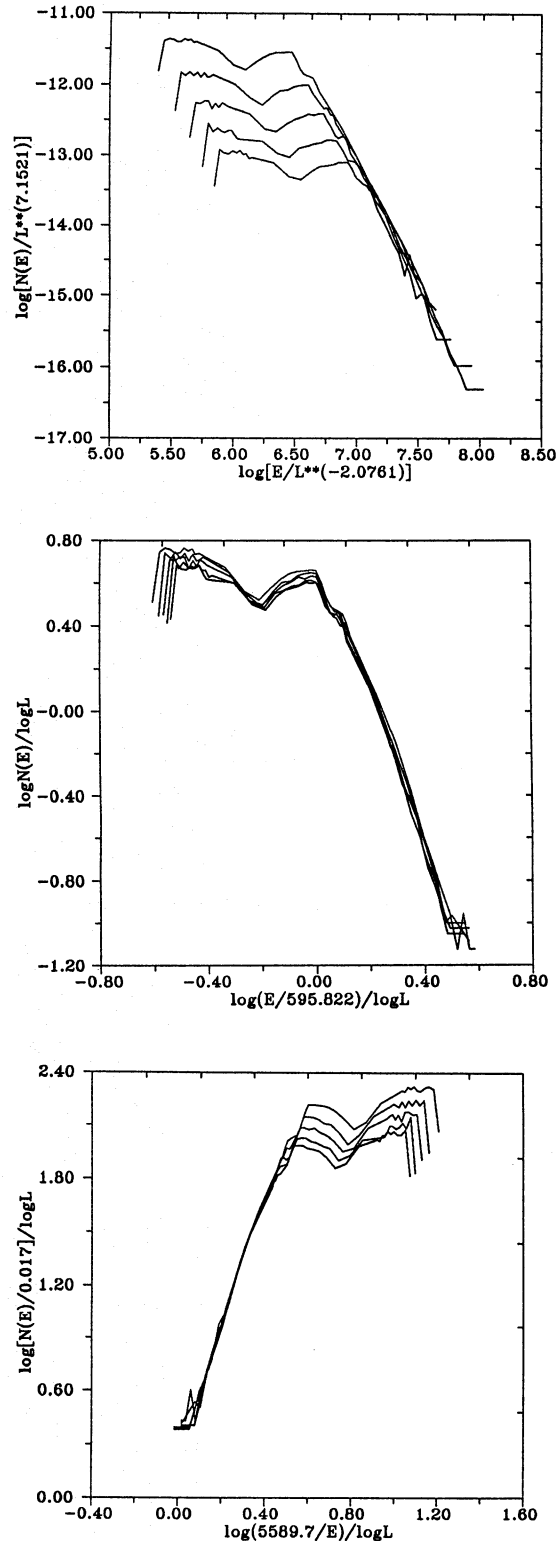

Fig. 11a–c. Scaling fits for energy distributions (L=60, 70, 80, 90 and 100) of Model B: **a** Finite-size scaling fit, **b** Multiscaling fit, and **c** Multifractal scaling fit. The multi-scaling fit works very good, the deviations in the lower-energy part are relatively small. The multifractal fit works also good, but the deviations in the lower-energy part are slightly bigger as compared to the multiscaling fit. The finite-size scaling fit works only good in the sharp power-law fall-off region

becomes unstable, the entire region is affected and the first- and second-order neighbours will have reduced instability thresholds. In other words: the instability criterion for the neighbours differs from the instability criterion of the initial unstable point. We assumed that there is a direct connection between the steepness of the initial gradient and the reduced instability thresholds of the neighbours. These instability criteria were developed by us in order to simulate highly unstable neutral sheets injecting energy into their environment in the form of jets and shock waves and forcing the entire neighbourhood to become unstable as well. Notice that the scenario presented here for the formation of flares differs from the view of Parker (1989) who suggested that microflares are the superposition of nanoflares and flares the superposition of microflares.

2. We introduced a new model called the "anisotropic model". In this model the initial instability criterion is applied to all six neighbours and the readjustment is done only with those neighbours satisfying this criterion. It is obvious that in this model the energy is redistributed anisotropically and it is much easier to satisfy the instability criterion. This change on the original model effects strongly the peak-luminosity power-law index.

3. Finally, we introduced a "mixed" model which combines the characteristics from the isotropic and anisotropic model. We expect this model to be closer to the realistic situation since we believe that inside an inhomogeneous active region both anisotropic and isotropic events will appear simultaneously.

Our results are the following:

1. We confirmed the results of LH with our isotropic model (a power-law behaviour in the peak-luminosity distribution with index ~ -1.8). The new instability criteria introduced in this article do not change the power-law index but create much larger avalanches and extend the range of the power law by several orders of magnitude. Our isotropic model then provides much bigger flares without changing the form of the luminosity distribution.

2. Our anisotropic model provides much smaller events (nanoflares) with a power-law index ~ -3.5 for the peak-luminosity distribution.

3. The mixed model is much closer to the realistic evolution of the active region. In Fig. 2a we observe points where the isotropic redistribution of the magnetic field will be proper (e.g. point (5,7) marked as I) and points where the anisotropic redistribution of the magnetic discontinuity will be in action (e.g. point (8,4) marked as A). This model provides simultaneously flaring and coronal heating, and the peak-luminosity distribution exhibits a double power law.

4. We used multifractal theory in order to investigate the occurence of correlations in our peak-luminosity time series. We found that this approach is quite successful and that correlation effects are strongly model dependent. We recommend the same method of analysis for observational time series. In this way new models can be more accurately compared with observations, rather than only comparing power-law indices. Our models A and C display relatively strong correlations, indicating the presence of memory effects in these model systems: the time evolution of these systems is affected by the past.

5. Our models exhibit a length-scale invariant behaviour in terms of the energy-distribution function. This implies that the size of the simulation boxes will not affect the phenomena reported here.

We demonstrated that this new approach of studying the energy release process in an active region is quite successful. It provides no information about the microscopic features of an individual event, but it gives very important information about the overall characteristics of its evolution.

Furthermore, we have shown that flares and nanoflares are governed by different relaxation mechanisms, but that these different mechanisms can be derived from one model using the same basic philosophy for the relaxation of magnetic field taking place in two different ways (isotropically and anisotropically).

The models presented in this article are still a long way from a realistic representation of the evolution of the active region. We consider our attempt here to be the first step in achieving this goal. The main drawbacks of our present modelling are the following:

1. Models A, B and C should be replaced by a single model which is able to apply isotropic as well as anisotropic relaxation criteria. This future model should treat each discontinuity separately. If a single grid point i satisfies the instability criteria with all its neighbours, it will relax isotropically. Otherwise the anisotropic relaxation will be applied. Instability Criteria I and II will be replaced by only Criterion II. This model will bring together all the important features of this study and is currently in preparation.

2. The discontinuities analysed in this article are the simplest possible for a magnetic field. Treating the magnetic field as a vector field will provide a number of new and interesting types of discontinuities (sheared fields, neutral sheets etc.).

3. The relaxation process should also become more realistic. A way to achieve this is the following: One can use simple 3D MHD simulations to study separately the evolution of several types of discontinuities. The redistribution of magnetic field, the released energy and the effects on the neighbourhood should then provide more realistic criteria for future models.

Finally, we conclude this article with the following remarks: Radiation signature models and particle acceleration processes can be developed in parallel in highly inhomogeneous and complex systems (see Vlahos & Raoult 1994; Anastasiadis & Vlahos 1994; Vlahos 1994). We expect that in the future energy release, particle acceleration and radiation will be modelled using complex-systems theory, following at the same time the global evolution as reported by observations.

We believe that the peak luminosity distribution of less energetic phenomena like decimetric spikes and type I storms will be better candidates for the diagnosis of anisotropic relaxation and steep power laws. We also hope that the results of the upcoming

SOHO satellite will prove useful in understanding the details of the statistical flare and its connection to coronal heating. It will be interesting to see if, after several decades of research on the "big flares", our understanding of the flare process may come from the other end of the spectrum, e.g. nanoflares and microflares.

Appendix A

In this appendix we introduce two new instability criteria as compared to the LH model. Both criteria share the same philosophy: neighbours of an unstable point have relaxation criteria which depend on the strength of the instability of the initial point. The steeper the gradient, the easier the triggering of the neighbourhood is. Criterion I involves only first-order neighbours, while Criterion II takes first- and second-order neighbours into account.

1. **Criterion I**. We define as the strength d_i of the instability at grid point i the difference between the slope at that point and the critical threshold, namely

$$d_i = dB_i - B_{\mathrm{cr}} . \tag{A1}$$

   For the first-order neighbours we define a (lowered) critical threshold

$$B'_{\mathrm{cr},i} \equiv (1 - \mathrm{dif}_i) B_{\mathrm{cr}} , \tag{A2}$$

   where dif_i is given by

$$\mathrm{dif}_i = A_1 \frac{\mathrm{nint}(d_i - 0.5)}{\mathrm{int}(d_i + 1.0)} . \tag{A3}$$

   Here $\mathrm{nint}(d_i - 0.5)$ is the integer nearest to $d_i - 0.5$ and $\mathrm{int}(d_i + 1.0)$ is the integer part of $d_i + 1$. A_1 is a free parameter which in all of our simulations was kept the same ($A_1 = 0.5$). It is clear that the new threshold $B'_{\mathrm{cr},i}$ is lower than B_{cr} and depends on the instability d_i in such a way that big gradients give rise to small $B'_{\mathrm{cr},i}$.

2. **Criterion II**. Criterion II provides a further extension of Criterion I. For the second-order neighbours we define a critical threshold

$$B''_{\mathrm{cr},i} \equiv B'_{\mathrm{cr},i} + A_2 B_{\mathrm{cr}} , \tag{A4}$$

   where the free parameter A_2 was kept constant in all our simulations ($A_2 = 0.3$). It is clear that this second-order threshold is bigger than the first-order threshold and depends on the strength d_i. (Making the second-order threshold smaller than the first-order threshold would correspond to an unphysical situation, since avalanches should not propagate forever.)

Appendix B

In the $f(\alpha)$ formalism for multifractals (Halsey et al. 1986), the support S on which a probability distribution is defined is partitioned according to

$$S = \bigcup_\alpha S_\alpha . \tag{B1}$$

Here α is the Lipschitz-Hölder exponent or singularity index associated with the probability distribution: if one covers S with a uniform grid of boxes with dimensionless box size

$$\varepsilon = \lambda / L , \tag{B2}$$

(L denotes the size of S), λ the size of a box and $\varepsilon \ll 1$), then all the boxes covering S_α have the same probability

$$P(\alpha, \varepsilon) \sim \varepsilon^\alpha , \tag{B3}$$

and the number of boxes covering S_α is given by

$$N(\alpha, \varepsilon) \sim \varepsilon^{-f(\alpha)} . \tag{B4}$$

The exponent $f(\alpha)$ is the fractal dimension of S_α. The graph of f versus α is usually a concave function and is called the $f(\alpha)$ spectrum of the multifractal. The $D(q)$ spectrum (spectrum of generalised dimensions) of the multifractal can be obtained from the $f(\alpha)$ spectrum using a Legendre transformation.

Now, setting $\lambda = 1$ in Eq. (B2), Eqs. (B3) and (B4) take the form:

$$P(\alpha, L) = c_1 L^{-\alpha} , \tag{B5}$$
$$N(\alpha, L) = N_0 L^{f(\alpha)} , \tag{B6}$$

where c_1 and N_0 are constants. The choice $\lambda = 1$ corresponds to a typical numerical-simulation situation: boxes covering a part of a lattice cannot be smaller than the unit box. The only way to decrease ε is to increase L, the size of the lattice.

If X is the typical physical quantity associated with the probability distribution, i.e.

$$X(\alpha, L) = c_0 P(\alpha, L) \text{ where } c_0 = \sum_\alpha X(\alpha, L) , \tag{B7}$$

then Eqs. (B5) and (B6) can be rephrased as follows:

$$X(\alpha, L) = X_0 L^{-\alpha} , \tag{B8}$$
$$N(X, L) = N_0 L^{f(\alpha)} , \tag{B9}$$

where $X_0 = c_0 c_1$ is constant. From these last two equations one straightforwardly derives the multifractal scaling form:

$$\frac{\log(N(X, L)/N_0)}{\log L} = f\left(\frac{\log(X_0/X)}{\log L}\right) . \tag{B10}$$

Note: the multifractal scaling form, when used as a fitting form, is selfconsistent when applied to models A, B and C (section 5): shifting the curves to the positive α-region results in positive $f(\alpha)$'s (Figs. 10c and 11c), whereas the multiscaling fitting form (21) gives rise to negative $f(\alpha)$'s (Figs. 10b and 11b). Though negative fractal dimensions are not strictly forbidden (Mandelbrot 1991), they are considered to be unphysical.

References

Anastasiadis, A. and Vlahos, L.,1994, ApJ. 428, 819

Bak, P., Tang, C. and Wiesenfeld, K., 1987, Phys. Rev. Lett. 59, 381

Bak, P., Tang, C. and Wiesenfeld, K., 1988, Phys. Rev. A. 38, 364

Bak, P. and Chen, K., 1991, Sci. American, January, p.26

Barber, M.N., 1983, in: Phase Transitions and Critical Phenomena, edited by C. Domb and J.L. Lebowitz, Academic, London, Vol. 8, p. 144

Berger, M.A., 1993, Phys. Rev. Lett. 70, 705

Berger, M.A., 1994, Spac. Sci. Rev. 68, 3

Biesecker, D.A., Ryan, J.M. and Fishman, G.J., 1994, ApJ., in press

Crosby, N.B., Aschwanden, M.J. and Dennis, B.R., 1992, Solar Phys. 143, 257

Dennis, B.R., 1985, Solar Phys. 100, 465

Eunaudi, G. and Velli, M., 1994, Space Sci. Rev. 68, 93

Fisher, M.E., 1971, in: Critical Phenomena, Proceedings of the International School of Physics "Enrico Fermi", Course 51, Varenna, Italy, edited by M.S. Green, Academic, New York, p. 1

Galsgaard, K. and Nordlund, A. 1994, Space Sci. Rev. 68, 75

Halsey, T.C., Jensen, M.H., Kadanoff, L.P., Procaccia, I. and Shraiman, B.I., 1986, Phys. Rev. A 33, 1141

Hentschel, H.G.E and Procaccia I., 1983, Physica D 8, 435

Heyvaerts, J., 1990, in: Basic Plasma Processes on the Sun, edited by E.R. Priest and V. Krishan, Kluwer, Dordrecht

Hudson, H.S., 1991, Solar Phys. 133, 357

Kadanoff, L.P., Nagel, S.R., Wu, L. and Zhou, S., 1989, Phys. Rev. A 39, 6542

Lin, R.P., Schwartz R.A., Kane, S.R., Pelling, R.M. and Hurly, C.C., 1984, ApJ 285, 421

Lu, E.T. and Hamilton, R.J., 1991, ApJ 380, L89

Lu, E.T., Hamilton, R.J., McTierman, J.M. and Bromund, K.R., 1993, ApJ 412, 841

Mandelbrot, B., 1991, Proc. R. Soc. Lond. A 434, 79

Parker, E.N., 1983, ApJ 264, 642

Parker, E.N., 1988, ApJ 330, 474

Parker, E.N., 1989, Solar Phys. 121, 271

Pearce, J., Rowe, A.K. and Yeung, J., 1993, Ap&SS 208,99

Priest, 1992, in: Eruptive Solar Flares, edited by Z. Svestka, B.V. Jackson and M.E. Machado, Springer Verlag, Berlin, p. 15

Sudan, R.N. and Longcope, D.W., 1992, in: Electromechanical Coupling of the Solar Atmosphere, edited by D.C. Spicer and P. Macneice, AIP, New York, p. 100

Tél, T., 1988, Z. Naturforsch. 43a, 1154

Van Ballegooijen, A.A., 1986, ApJ 311, 1001

Vlahos, L., 1994, Space Sci. Rev. 68, 39

Vlahos, L. and Raoult, A., 1994, A&A, submitted

Withbroe, G.L. and Noyes, R.W., 1977, Ann. Rev. Astr. Astrophys. 15, 363

Zirker, J.B., 1993, Solar Phys. 148, 43

Zirker, J.B. and Cleveland, F.M., 1993a, Solar Phys. 144, 341

Zirker, J.B. and Cleveland, F.M., 1993b, Solar Phys. 145, 119